Technical Design Report

Report prepared by:
Shivam Dixit, Aerodynamics Lead
Eleni Daskopoulou, Electronics and Controls Lead
Ariana Diaz, Generator Lead
Kaitlyn Shaughnessy, Structures Lead
David Corrente, Team Lead

With guidance from Dr. Dennice Gayme and Dr. Rui Ni, Faculty Advisors

<p style="text-align: center;">**Table of Contents:**</p>

1 Executive Summary

The JHU team's goal for the 2024 Collegiate Wind Competition was to design and build a unique off-shore wind turbine which optimizes its power output and efficiency within the given structural limits of the competition's rules and requirements. Specifically, we are aiming to achieve an increase in performance on the testing section of competition when compared to our performance last year.

The turbine blades are modeled from the S1210 airfoil at the tip, S1221 airfoil in the middle, and FX63-137 airfoil at the root, with added winglets and vortex generators for an increased and consistent power production. They were tested on a turbine structure and with a static failure test. The final blades were 3D printed out of PLA filament.

We chose a new off-the-shelf motor, the Nanotec DFA90L048017-A, based on marked improvement when compared against the Lin Engineering BL423E48. The new motor performed better than last year's in theoretical power generation, and this was later confirmed with empirical testing in the wind tunnel. Additionally, we designed and built a custom generator which matches the dimensions and profile of this motor for easy system integration and testing.

The turbine is operated by a microcontroller-- located inside the nacelle--which monitors the turbine's performance by measuring: RPM, current, and voltage. The microcontroller then uses these inputs to actuate relevant controls. Pitch is directly controlled by the turbine microcontroller while the desired load resistance is adjusted by the laid electronics. For the safety task, braking is accomplished by feathering while back-up power is provided to the turbine through a custom power management unit.

The foundation supporting the turbine is a spur-bucket design with inspiration taken from last year's caisson-type foundation. The nacelle was modified to fit the new structure of the generator and make accessing electronic components easier when compared with last year's design.

2 Technical Design

2.1 Design Objective

For the 2024 Collegiate Wind Competition, we aimed to explore new design concepts and alternative ways for accomplishing the competition tasks. We prioritized rapid prototyping to determine the feasibility of new ideas and evaluated the experimentation results on performance baselines established through previous competition designs. This process yielded significant changes in some turbine subsystems, while in others, it validated the selection of more established, previously used designs. To broaden our understanding of generator operation and parameter optimization, we designed and built a custom generator. For blade optimization, we investigated the effects of features like vortices and winglets. To design the foundation, we performed scale testing on various foundation types to determine the strengths of each. Finally, for the electronics, we leveraged the speed and reliability of hardware-based control systems for our safety system, and developed more sophisticated software-based control schemes for power optimization.

Power: 0.0480713 kW
Cp: 0.540446
V_in @ hub: 10 m/s

2.2 Rotor and blades

2.2.1 Blade Design and Analysis

Our main goals for blade design were to prevent blade failure and to improve aerodynamic performance from our previous designs. We researched airfoils suitable for small-scale wind turbines and simulated blades with airfoils due to their high and consistent C_L/C_D at low Reynolds numbers [1].

Previously, we set the blade length to 18 cm and the hub radius to 3.5 cm, within the competition specifications. We split this length into 20 discrete sections. Testing data indicated
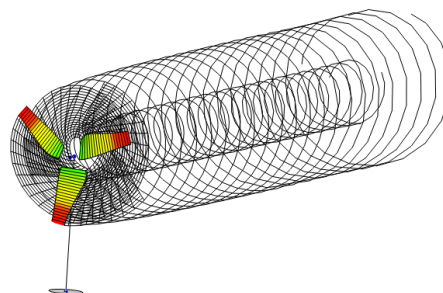

Figure 1. LLT Simulation of blade at 10 m/s

consistent performance at an optimized TSR of 3, which informed our decision to redesign for this TSR. We generated airfoil polars for Reynolds numbers of 37000 and 50000 (typical for small-scale wind turbines). The chord length and twist angle of the blade were chosen using QBlade's Schmitz optimization method. We researched and simulated multiple low-Reynold's number optimized airfoils, such as the SD2030, SG6403, and S1223, in QBlade's lifting line theory simulation at different wind speeds between 5-11 m/s. The S1221 airfoil improved the power coefficient of the airfoil combination used in CWC2023 by 10% in the simulations, so we chose it in combination with the S1210 airfoil at the tip and FX63-137 airfoils at the base *(Figure 2)*. This blade yielded a power coefficient of around 0.54 at 10 m/s in LLT simulations *(Figure 1)*.
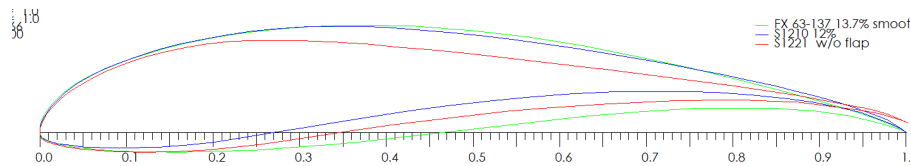

Figure 2. Airfoil sections for FX63-137, S1221, S1210

2.2.2 Performance Testing

We conducted tests with this blade in JHU's wind tunnel at integer speeds between 5-11 m/s for power production. Our previous rotor hub, the JCZK 300RC helicopter rotor hub [4], is being used to pitch the blades due to its familiarity and ease of use. The linear actuator is attached to the rotor hub using a 3D-printed mount. The power and RPM were recorded at different pitches for each wind speed to determine the maximum possible power production. The results showed a 5% improvement in average power produced by the blades over last year's design.

2.2.3 Winglets and Vortex Generators

During our research, we came across retrofit methods to improve the performance of turbine blades, such as winglets [2] and vortex generators [3] *(Figure 4)*. Winglets are meant to reduce drag by reducing the size of tip vortices, thereby increasing C_L/C_D

Figure 3. Power score comparison of blades with vs without winglets

. Vortex generators postpone the stall angle of the blade by delaying flow separation at the boundary layer of airflow over the blade. We tested blades with these features to determine whether they made a significant difference to aerodynamic performance. While the vortex generators did not have an impact on performance, they consistently kept the blades close to peak performance over a larger range of pitches, at lower speeds, reducing the chance that any errors in pitch angle would significantly affect performance at these speeds. With the winglets, we saw an 11% performance enhancement over wind speeds from 5-11 m/s *(Figure 3)*.
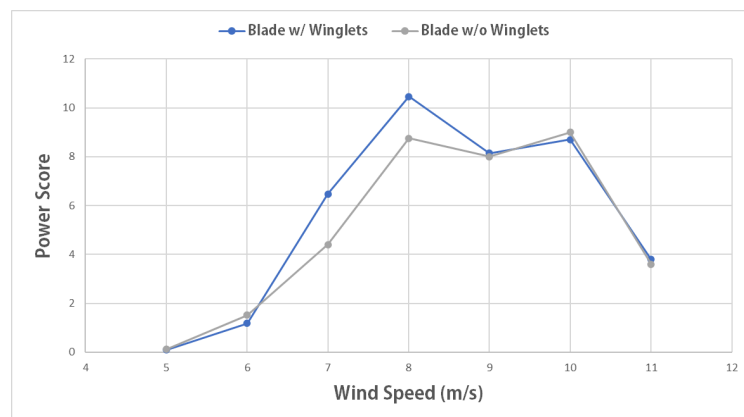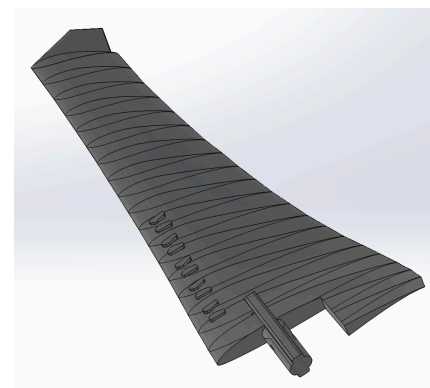
2.2.4 Structural Testing

Figure 4. Blade with winglet and vortex generators

Our rotor hub connection piece was at a minimal risk of failure under both normal and stressed operating conditions. However, we observed failure during the testing phase of CWC2023 due to abnormally high RPMs (>3000) during the durability task. As a result, we designed and printed blade designs with a more robust rotor hub connection piece. Theoretically, it would be able to withstand much higher bending and centrifugal loads as seen in the simulation results below (*Appendix C*). This also reinforced vertically-oriented prints–yielding a much smoother surface finish–but had significantly lower strength as the normal loads were maximum along the blade's span. We observed failure of a vertically oriented blade made of PLA with the retrofit winglet at the blade root. This failure was characterized by shearing between the print layers, further reinforcing the need to test the new rotor hub connection design.

We conducted testing to validate both the strength and durability of the rotor hub connections, as well as whether the new rotor hub connection design had any significant effect on performance. *Figure 5* shows the expected load distribution over the blade, calculated using extracted vector wind-field data from QBlade and MATLAB calculations for thrust and drag forces on each section of the blade. These calculations were then used to conduct an FEA analysis on blades with both hub connection geometries with centrifugal and bending loads.
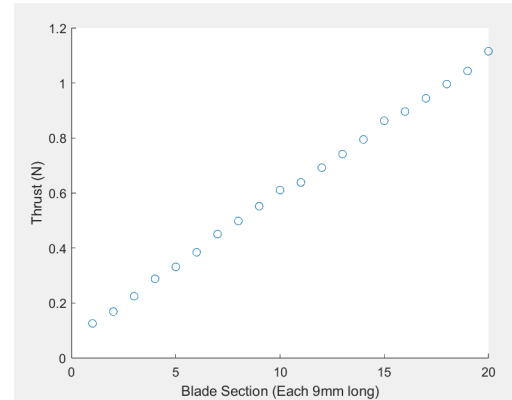
Figure 5. Load distribution over blade at 11m/s

Static failure tests were conducted to validate material and 3D print orientation strength. The blades were 3D printed with either the BambuLabs X1 Carbon with PLA, ABS filaments due to their ease of manufacturing or the Stratasys F370 with Polycarbonate-ABS blended filament, due to its high layer adhesion and strength. The blades were strung at three points along its length to simulate a distributed load *(Figure 6)*. The horizontal prints are layered spanwise, while the vertical prints are layered chordwise. Our results led us to print our final blades with PLA filament in the horizontal orientation. While the resin and ABS have higher safety factors, PLA resulted in a smoother and more consistent print overall. The new hub connection geometry (surrounding) has a higher safety factor, but we deemed that it was unnecessary to compromise on the performance of the blade due the larger geometry.
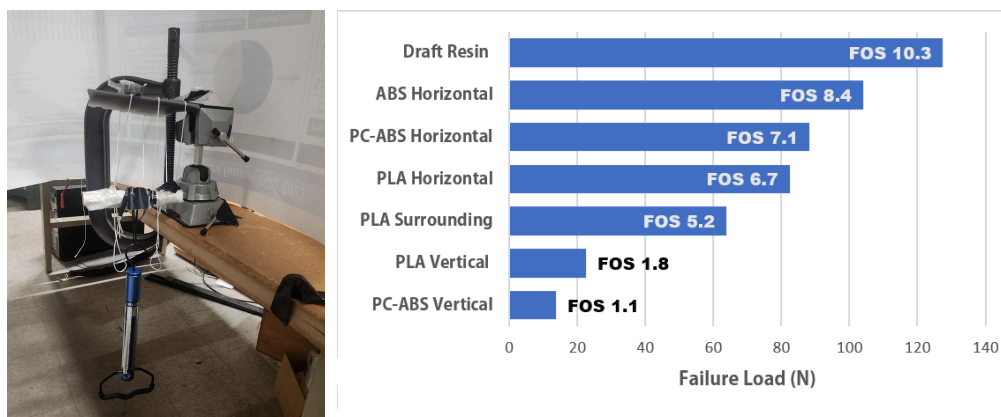
Figure 6. Static bending test setup for blades (left) and results (right)

2.3 Generator and Powertrain system

2.3.1 Motor Theoretical Testing

We have decided to reevaluate our motor choice and continue testing new off-the-shelf motors as we did last year. In particular, we looked at theoretically modeled performance compared to our previous motor, the Lin Engineering BL423E48.

The model that we created uses the input torque and RPM as well as known motor characteristics such as the torque constant, back EMF constant, and the winding resistance to predict the power losses and total power generated at each wind speed. Power production before losses was calculated using the motor constants:

$$P_{raw} = IV = \frac{k_T}{T} \cdot k_v \, \omega \tag{1}$$

where P_{raw} is the raw generated power before losses, I is the current, V is the voltage, k_T is the torque constant of the motor, k_v is the back EMF constant of the motor, T is the torque from the blades, and ω is the rotor angular velocity.

The losses due to joule heating in the generator were also calculated at each windspeed as:

$$P_{heat \, loss} = I^2 R_{winding} \tag{2}$$

where $P_{heat \, loss}$ is the power lost due to joule hearing in the generator, and $R_{winding}$ is the internal winding resistance of the generator.

We did not have an accurate way to predict the frictional losses non-empirically, so we assumed a constant 12% frictional loss based on prior research and testing for last year's generator. We then calculated the expected power output at each wind speed from 5-11 m/s.

At the highest wind speed, the BL423E48 would theoretically produce 23.8W, while the DFA90L048017-A would produce 31.4W. This is a theoretical performance increase of 32%.

2.3.2 Motor Empirical Testing

To simulate competition conditions as closely as possible, we created a wind tunnel test stand out of T-slot framing *(Figure 7)* that held our powertrain including blades, bearings, encoder, linear actuator pitch control, and a variable load resistor. This design allowed us to 3D print different generator mounting pieces and switch out generators without changing the rest of the setup.

The empirical motor testing provided us data on the motor's output voltage, current, and resulting power as a function of the blade pitch and the load resistance. The blade pitch was varied using an RC helicopter rotor hub and a 5V linear actuator (boosted with 6V input to stabilize the held pitch angle with a larger output force from the actuator). The load resistance was varied using a cement potentiometer (0-50 Ohm). Our results with this year's selected motor (DFA90L048017-A) were similar in trend to last year's motor. The main difference is power output at each wind speed.

The load resistance directly changes the motor's constants, and gives a complex result which is difficult to theoretically model. By increasing the load resistance by a small amount (with a potentiometer in series with the motor's rectified output) the rectified output voltage decreases, the rectified output current increases, and the motor's RPM under constant torque decreases compared to running the motor with no additional load. *Figure 8* showcases the data collected during the power generation optimization tests. The results shown from the surface plot indicate that generally a linear actuator position of 1200 for the blade pitch and an in-line resistance of 7-8 Ohms results in the highest generated power at a wind speed of 9 m/s. These results are similar across all wind speeds, with notable differences being centered around a changed load resistance rather than an alternative pitch.
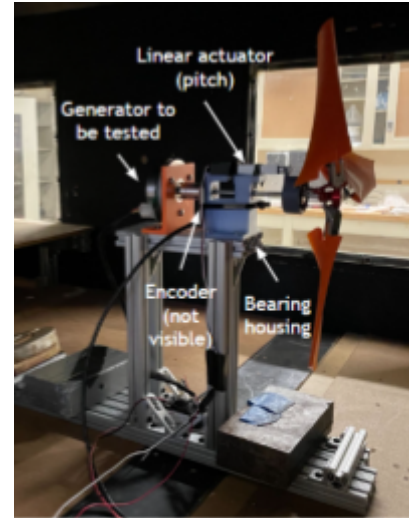

Figure 7. Wind tunnel test stand

When testing the new motor with winds up to 11 m/s, we observed a maximum power output of 55.3W, which is an improvement from last year's result of 24.3W *(Table 1)*. This is a performance increase of 127%. When compared to the theoretical output of the motor under wind speeds of 11 m/s, the motor performed 76% better, producing 21.9 W higher than expected. This scale of performance improvement has not been seen in any other motor that we have tested in the past, however the test has been completed several times in order to verify the results. We currently are not certain as to the reason for such a marked increase in performance, but have determined the optimal values of pitch and added load resistance in order to maximize the motor's performance at each wind speed.
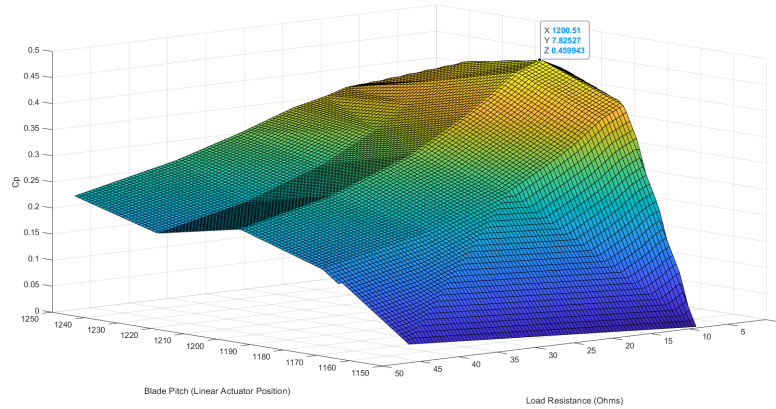

Figure 8. Example C_P vs. pitch and load resistance plot from wind tunnel test at 9 m/s

Table 1. Maximum power generated at each wind speed for each motor with estimated power score

Motor Tested	Power generated at each wind speed (W)							Calculated Power Score
	5 m/s	6 m/s	7 m/s	8 m/s	9 m/s	10 m/s	11 m/s	
BL423E48	1.77	4.13	8.03	11.37	16.24	23.04	29.67	35.3
DFA90L048017-A	4.61	10.41	17.21	27.05	30.64	43.23	55.28	75

2.3.3 Design of Custom Motor

In addition to testing off-the-shelf motors, we have begun to lay the groundwork for developing and using our own custom generators. We have iteratively designed a motor which matches the dimensions of our newly selected motor, such that we could quickly substitute them out without modifying any other system component. We have chosen a radial flux design to satisfy both our easy integration requirement and for ease of manufacturability. Our design features a stator with 32 poles that can fit copper wiring coiled in alternating directions. A rotor seats 32 corresponding magnetics which we have salvaged from another already existing motor. This part also has a set hole which allows a shaft to be connected to the linear actuator in the final positions set up. Together *(Figure 9)* these two halves comprise our custom design.

All parts of our design were 3D-printed in PLA using a Prusa i3 MK3S+ 3D Printer so that we could easily make minor changes based on design flaws we encountered during assembly and testing. As a result, we completed many iterations which improved overtime. When optimizing our design, we wrapped the wires within two sets of coils in series. Each pole was wrapped in 14 clockwise coils, the coiling sets alternating with one another, each covering 16 poles. This two-coil-set-layout allowed the current between poles to be generated in the same direction, preventing destructive interference due to adjacent, opposing current directions. We opted for higher gauge wire to increase the max current the motor is capable of maintaining; this matches the modeling we used for our motor selection. Additionally, to improve the function of our generator we moved to printing out of a magnetic 3D print filament. This increased the magnetic flux as per Faraday's Law, which in turn increased the induced current. Using the same test set up from motor selection, we tested our custom model and were able to achieve a maximum power generation of 55.28W. This clearly did not exceed our chosen motor; however, is a good foundation for

future iterations of our generator design. In the future, we hope to improve our manufacturing methods such that we can use metal for our rotor and stator and move away from rapid prototyping to achieve a more permanent and effective custom generator.
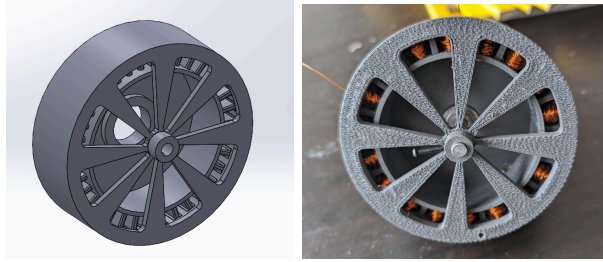

Figure 9: CAD Model and Prototype of Custom Generator

2.3.4 Converting and Stabilizing Power

We generate a DC voltage by converting the DFA90L048017-A 3-phase AC-voltage output through a full-wave rectifier. In order to avoid instability due to periodicity, we added a low pass filter; a parallel capacitor connected to the power and the generator suppresses any oscillations which may propagate--preventing interference with our PCC and our load. We found that the relatively stable DC voltage is produced by maximizing the converted power. As per competition rules, we allow for a fluctuation of ±10% in power (or ±10% in voltage) variation. This corresponds to a V_{pp} of 0.45V at a wind speed of 5 m/s. We found a frequency of 22 Hz (*Equation 3*) and a minimum capacitance of 0.028F (*Equation 4*).

$$f = 120 \times poles \times rpm \tag{3}$$

$$C = \frac{I}{2fV_{pp}} \tag{4}$$

where I is 0.55 A.

2.4 Electronics and Controls

The electronics and controls are both the hardware and firmware developed to optimize the specified competition tasks. They are divided into two critical subsystems: the turbine electronics which are located inside the nacelle, and the load electronics that simulate the power grid. Sensor inputs are collected from the turbine, processed by the on-board turbine processor and control outputs are adjusted accordingly on either the turbine or load side. The migration to a single microprocessor in the turbine was done to eliminate unnecessary complexity and eliminate the need for microcontroller communication. The processor we selected is an ESP32 core for its low footprint and power consumption along with the additional wifi capabilities. The turbine electronics are powered by the turbine-generated power, while the load electronics are powered by wall power. There are 4 signal connections between the turbine and load electronics: two for the safety system and two for I2C communication. All connections are optically isolated using optocouplers which utilize a photodiode and a phototransistor to convert the electrical signals to optical and then back to electrical.

2.4.1 Turbine Optimization Controls

The main functionality of the turbine side microcontroller is the collection of data to detect the mode of operation (power optimization, rated power, durability) and optimize the controlled variables (pitch, load resistance).

One of the tasks we found the most difficult last year was accurately measuring the wind speed to perform the above functions. To address that, we proceeded with two design changes. To be able to differentiate between wind
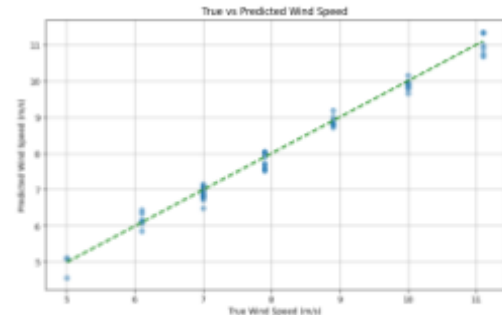

Figure 10. Deviation between measured and predicted wind speed acquired from the linear model

speeds, we collected RPM data at varying pitch angles, load resistances and wind speeds. We then trained a machine learning model using linear regression. We acquired an equation for wind speed as a function of RPM, pitch, and resistance. We are able to predict the wind speed with an error up to 5% of the value measured by an external anemometer *(Figure 10)*. This system, despite requiring extensive measurements to train and calibrate, is robust to sensor noise and turbulence effects from the blades.

For power optimization, instead of having predetermined optimal configurations, we adopted a real-time optimization algorithm that is agnostic to wind speed. More specifically, we utilize a "perturb and observe" maximum power point tracking (MPPT) algorithm to dynamically change the load resistance. We use a power monitoring sensor to measure the voltage and current and compute the turbine's instantaneous generated power. To adjust the load resistance, we designed a new high-power variable load that can be precisely controlled by the turbine microcontroller through hardware based feedback loops. The circuit uses a combination of high power resistors and transistors to draw a specified current in the range of 0-4A *(Figure 11)*. The analog nature of load resistance allows us to effectively use it for the implementation of the MPPT algorithm.
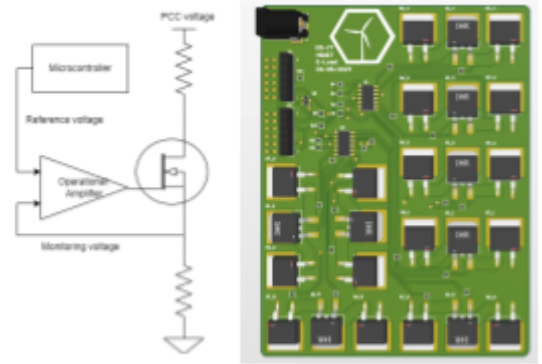
Figure 11. Multiple channels were connected in parallel to increase the current dissipation capacity

Through integrated testing, we determined that the optimal pitch for each wind speed in the range 5-11m/s doesn't significantly affect power generation, so we decided to keep blade pitch constant for the power optimization test to simplify controls. For the rated power task though, we use an opposite control scheme, keeping the load constant and actively pitching the blades to maintain the desired power and RPM in the range of 11-14m/s. This rated power control scheme is also implemented during the durability task to keep the RPM within the structural limits of the turbine. Through wind tunnel testing we developed a PID controller that measured RPMs using an encoder and controlled the pitch through a pulse width modulated signal to a linear actuator. The controller was tuned to minimize response time and reduce oscillations *(Figure 12)*.
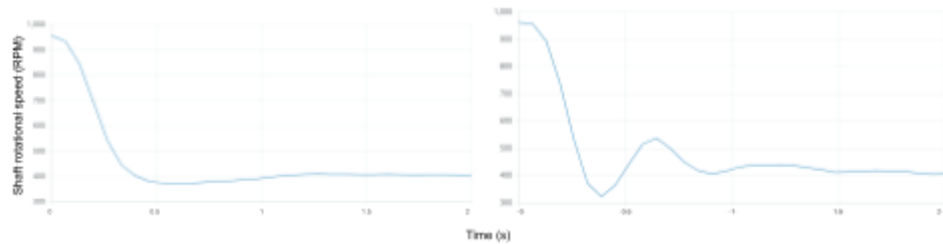
Figure 12. Testing the response of different PID controllers during an extreme fluctuation of the RPM from the desired value (400 RPM)

The active pitching system is also used as a protection against overvoltage. The motor is rated for 48V at 1670 RPM. In testing we had seen rotational speeds as high as 2415 RPM, which exceeds the generator's rated values. Based on the motor constants, this would be expected to output 58V (not accounting for losses). In order to keep the generator within the voltage requirement of 48V and below, the electronics will pitch towards the feathered position if the generated voltage surpasses 45V. Additionally, the load current draw will increase, ensuring a safe voltage even at those RPMS.

2.4.2 Safety System

The safety system is responsible for accomplishing the brake and restart task when the safety button is pressed or the load gets disconnected. To detect an emergency button stop, we apply 5V on one side of the switch through a pull-up resistor and read the voltage on the other. This signal is read by the turbine, which activates the braking mechanism when an open-circuit condition is detected. To detect a PCC

disconnect, an operational amplifier monitors the PCC voltage on the load side and produces a high signal when it falls below 5V. This condition should only occur if the PCC is disconnected or the turbine is braked due to an ongoing safety stop. All signal detection occurs using interrupts to make sure that safety related actions take priority over all other processes. The same circuit is responsible for providing backup power to the turbine to restart when necessary. The load is always powered by an 8V DC power source (connected to the wall power) that gets connected through a transistor to the PCC when the turbine is not operating. The analog nature of the above circuitry aligns with our primary goal of relying on hardware mechanisms to increase reliability and reduce the involvement of microcontrollers and more complex communication mechanisms which can introduce additional fault conditions.

The physical braking mechanism utilizes the linear actuator to feather the blades, which effectively drops the shaft rotations to a range of 0% (at low wind speeds) to 7% (at 11m/s) of the original speed. Given the effectiveness and reduced loading accomplished with the feathering based braking system, we decided to not pursue an additional mechanical brake.
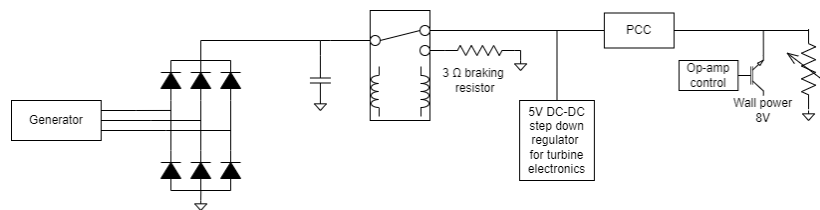

Figure 13. Powertrain diagram for turbine and load electronics

2.4.3 Firmware

To perform the operations described above, the turbine's operating principle is a state machine that operates under the different control algorithms based on the current mode of operation (normal operation, safety state, restart state) and the task that needs to be performed (optimized power, rated power).

Development of the above firmware was done incrementally by different members of the electronics team. Each sub-task's code development (safety, rated power, power optimization, sensor readings, load setting.) was performed and validated independently. We then reviewed each separate sketch and created functions that would abstract the hardware level of each component. That allowed us to continue hardware and software development of each separate task in parallel with combining all of the above functionality and creating the final state machine. Arduino libraries were used when available with the sensors and actuators selected. The final step was migrating from using Arduino Uno processors due to their availability and ease of use to our selected ESP processor. Once the firmware was tested on a benchtop setting, we moved to integrated wind tunnel testing simulating the competition conditions to evaluate performance and resolve any remaining bugs.
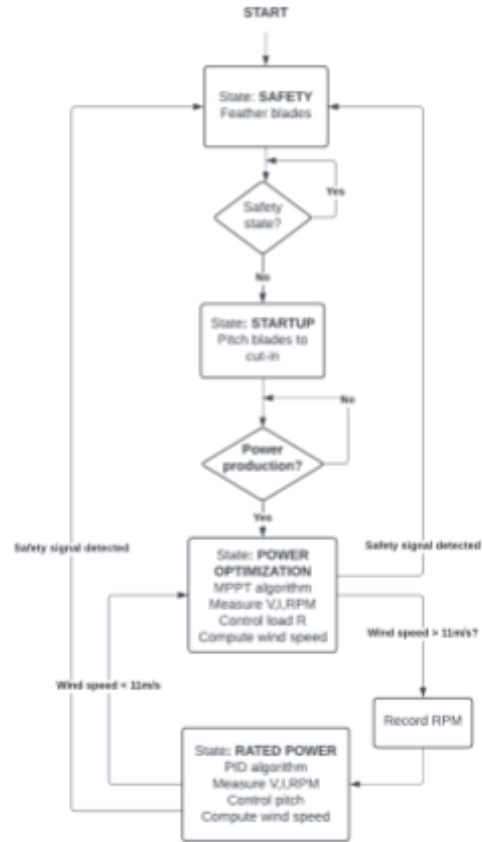

Figure 14. State diagram for turbine firmware

2.4.4 Monitoring Dashboard

To facilitate integrated testing, especially in cases where accessing the microprocessing through a serial wire is not possible, we decided to develop an online dashboard that will display the most important collected data in real time. This allows us to monitor the turbine's performance and verify that it operates as expected without interfering with it. For testing purposes only, the dashboard also grants control access to the turbine, allowing it to be a diagnostics and troubleshooting tool. To build the dashboard we utilized the wifi connectivity of the ESP32 microcontroller and developed a user interface in html and javascript.

Figure 15. Example snapshot from the dashboard during wind tunnel testing

2.5 Structures

The structures subsystem's goals centered around supporting the turbine in both stationary and operating conditions throughout the testing period, up to wind speeds of 22 m/s. The primary goals of the nacelle design were to increase accessibility to inside components, create an aerodynamic shape, and easily mount internal components.

2.5.1 Offshore Foundation Design, Fabrication, and Testing

Last year, the suction caisson foundation design was chosen over its more widely used counterpart, hollow monopiles, for its lightness, simplicity, and ability to introduce stress to benefit the foundation's strength. However, after a thorough analysis of past design reports, we concluded that the most successful foundation designs use the weight of the sand to help strengthen the foundation and prevent deflection. Thus, we developed a new design that combined last year's cassion base with angled spurs to screw into the sand, effectively reducing friction and anchoring the foundation in place.

When selecting the foundation material, we considered several factors, including strength, durability, structural integrity, and density. Though we considered composite materials due to their high strength-weight ratio, we eliminated this option quickly due to them not being a ferrous material and that steel is more widely used in industry. Thus, we decided to use stainless steel again for our foundation.

Figure 16. Final foundation design

Our final foundation design *(Figure 16)* includes a square bottom with a cylindrical side wall. The screws were designed in a circular pattern to align with the installation process, thus reducing friction while screwing the foundation into the sandbed.

The circular spurs and base plate were cut using a waterjet. The spurs were then bent to 15° to penetrate the sand. The baseplate is made out of 0.06" thick stainless steel to prevent bending of the spurs as they are turned into the sand. The foundation wall is made from 0.024" thick stainless steel, significantly thinner than the baseplate but easier to roll for manufacturing. The center tube of the foundation was cut to 35 cm to comply with the tolerances of the sandbed height to the top of the testing tank. The assembly was welded

Figure 17. Diagram of testing set up and real test set up

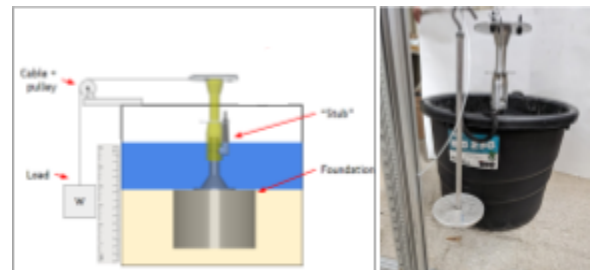together and small supports were added at the end of each spur to prevent deflection during insertion.

Since our entire turbine is unable to fit into our wind tunnel, we performed isolated static loading of the foundation. The testing tank was 22.5" in diameter by 16.5" tall and filled with sand and water depths stated by competition rules *(Figure 17)*. Next, using a meter stick to measure deflection, we loaded the foundation laterally until the stub was displaced by 25 mm. The static testing showed that the stub had its max deflection at 2700g of load. The theoretical max thrust at 22 m/s is calculated to be 2876g, so our foundation failed the static loading testing.

Theoretical analysis for the foundation showed promise for stability. In practice, the base was not able to penetrate the sand 20cm. As such, we iterated our design and created a caisson-similar design with the spurs moved to the top of the wall. This will allow for easier insertion to the sand by reducing the surface area being pushed into the sand. The current manufacturing of our iterated design is still in progress and will be tested before the competition. This new caisson design will be compared to the performance of our caisson from last year to determine the design with the most stability.

2.5.2 Yaw System Design

Since there is no yaw turntable incorporated into this year's competition, we decided to proceed with our set screw approach from last year. While previous testing suggested the lockable yaw system would be able to withstand the expected yawing moment of the turbine, in competition the set screws stripped and did not provide the holding power we needed. We've added two more support set screws to ensure holding power and distribute the load.

2.5.3 Tower-Base Assembly

For the selection of materials for the tower-base assembly, we created material indices for minimizing deflection and also minimizing mass. Modeling the tower as a cantilever beam, we found the material index $M = \frac{E^{1/4}}{\rho}$. We then plotted this material index on Granta with a slope of 4 for metals *(Figure 18)*.
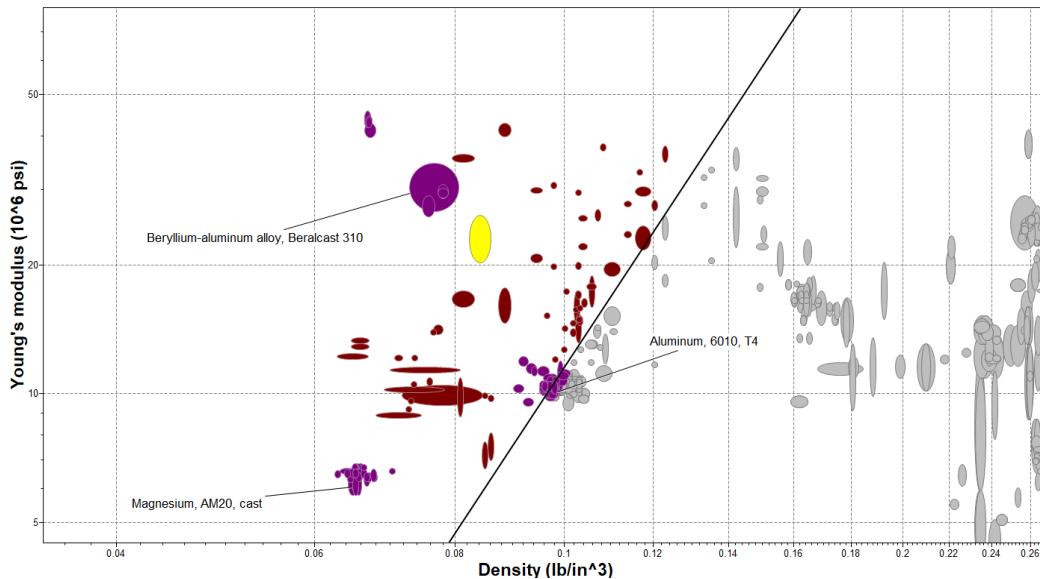
Figure 18. Ashby chart with Young's modulus on the y-axis, density on the x-axis, and a slope of 4.

We found that beryllium, magnesium, and aluminum stood out as the best options. Aluminum proved to be our best option again due to its low density while maintaining a high Young's modulus. Also, aluminum tubing and sheets are easily accessible to order through McMaster-Carr. The tower has a 1.5" ID and 2" OD to provide room for the electronic wires to run through the tube.

2.6 Enumeration of Influence of Previous Design Reports

Our performance in last year's competition has provided a strong foundation for exploring new design concepts and improving our overall turbine design.

Previous Year	Current Design
JCZK300RC Rotor Hub	Same rotor hub, easy to use and set to a precise pitch
Blade modeled from S1210 and FX63-137 airfoils (CWC23).	Blade modeled from S1210, S1221, FX63-137 airfoils to improve power coefficient.
Theoretical calculations motors for power production capabilities and chose BL23E22 model.	Improved theoretical motor comparisons and chose Nanotec DFA90L048017-A Designed Custom Radial Flux Generator.
Power relay based safety system.	New hardware based power management unit for providing back-up power.
Switch based parallel resistors variable load.	Analog-controlled transistor based.

2.7 Static Performance Analysis

2.7.1 Cp-TSR Curve

To test our performance at different loads, we tested our turbine with variable wind speeds from 5-11m/s, loads and pitches. We recorded the tip-speed ratio and power coefficients by finding the ratio between tip speed and wind speed, and ratio between generator output and power received from the wind. According to the data, the generator is more efficient at higher TSRs. The maximum power coefficient occurs at a tip speed ratio of 3.8 at an angle of attack of 6 degrees.

2.7.2 Annual Energy Production

The annual energy production of our turbine would vary significantly based on the installation location. If we install our offshore turbine in the great lakes, we can expect an average yearly wind speed of around 8.5 m/s. Given the highly non-linear relation between wind and power generation of our wind turbine we need to consider the distribution of wind speeds throughout the year. Using data from NREL's Eastern Wind Data Set [13], we can expect 0-5m/s wind speeds around 35% of the year, 5-8m/s for 45% of the year, 8-12m/s for 15% of a year and above 12m/s for the remaining 5%. This would result in an annual energy production of 139.3 kWh.

3 Full Turbine Integration

3.1 Integration

We prioritized ease of access to the generator and electrical components when designing the nacelle (*Figure 19)*. Our last nacelle design did not facilitate easy access to the generator or electronics when necessary (i.e. for component maintenance or replacement). We've opted for a removable top to the nacelle, such that we can place the assembled generator and electrical components down into the base of the nacelle, and then close the top. We 3D-printed the nacelle in 4 parts; the top and bottom main portions, and then the top and bottom nose pieces. The nose and bottom were connected using heat-set inserts and screws. In the center of the nacelle there are two T-slot rails that run through the middle of 80-20 for mounting. The generator is mounted onto the 80-20 outside of the nacelle, then placed in and secured with a screw from the bottom. We are using self-aligning bearings to support the shaft and prevent deflection at high rotational speeds.

Figure 19. Section View of Nacelle Mechanical Design

3.2 Distributed Team Management

Our team consists of four subsystems; the Aerodynamics, Generator, Electronics and Controls, and Structures subteams. Each team is managed by a lead who is responsible for the subsystem design and interface with other systems. Mutual progress is facilitated under the guidance of the team lead. With this hierarchical structure, people with multiple levels of experience can contribute to the overall progress while maintaining the necessary level of collaboration between different teams.

4 Assembly & Commissioning Checklist

Each Commissioning Task will be performed by a team member who will initial the list after completion. Each completed task will be verified by a team member who will also initial the checklist.

Before Timed Assembly	Performed by	Verified by
Gather all nacelle components: nacelle (3 pieces), turbine electronics, 2 mounts, 8020 frame, linear actuator, generator, encoder.	KS ___	SD ___
Place and connect all turbine electronics and peripherals in the nacelle.	ED ___	AD ___
Close the nacelle and fasten the screws.	KS ___	AD ___
Feed foundation wires (power + signal cable) through the foundation.	ED ___	SD ___
Assembly Task		
Thread cables through the stub. Hold the tower with the nacelle above the stub and clip the power and signal connectors.	ED ___	KS ___
Fold additional wire length in the tower, position on the stub and tighten wingnuts.	SD ___	AD ___
Orient the nacelle along the wind direction and secure in place.	ED ___	AD ___
Connect the following: - Load to PCC and Foundation to PCC power cables - Signal cable between foundation and load - Safety button to PCC - Load to wall power	ED ___	SD ___
Commissioning Task		
Press safety button to reset the turbine. Wait for turbine to pitch.	ED ___	KS ___
Unpress the safety button and wait for the turbine to pitch to start-up.	ED ___	KS ___
Request 5m/s wind speed. Verify proper power generation.	ED ___	KS ___
Request 11m/s wind speed. Note down RPM and power production.	ED ___	KS ___
Request 14m/s wind speed. Verify that RPM is the same as at 11m/s (+-5%).	ED ___	KS ___
Request 5m/s wind speed. Wait for blades to move to startup position.	ED ___	KS ___

5 Turbine Testing Results

5.1 Power Curve Testing

The Corrsin Wind Tunnel on the JHU Campus is a closed loop tuned with a 1m by 1.3 m test section which allows us to test up to 11 m/s. For our power curve testing, we ran tests up to 11 m/s using a tower shorter than our final design to accommodate the small height of this wind tunnel. Optimizing for pitch and load, we maximized power for wind speeds from 5 m/s to 11m/s at 1 m/s increments. We found our maximum power output to be 55.28 W at 11 m/s.
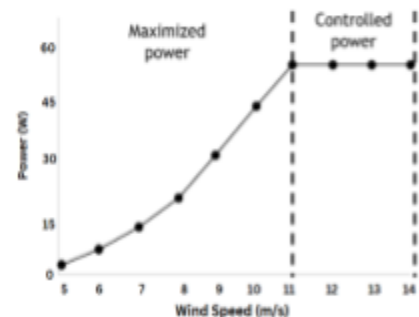

Figure 20: Power Production Curve

5.2 Durability

For wind speeds upwards of 11 m/s, we plan to test at the University of Maryland's (UMD) Glenn L. Martin wind tunnel. There, we plan to fully assemble the turbine including the foundation. This will be installed in a sand tank filled up to 25.4 cm. We will repeat our deflection testing, this time with the turbine active. For this test, we plan to take measurements using a ruler recorded by a camera. For wind speeds from 12 m/s to 22m/s we will try braking within 30 seconds via feathering. At 22 m/s we will run a 5 minute test for braking via feathering and while at 15 m/s we will test blade pitching. These tests will be run to determine the viability of our new foundation design. This will allow us to make our final design decision based on what was discussed in the structure section of this report.

6 Appendix
6.1 Appendix A: Expected mechanical loads and safety factors

Part	Load case	Expected load	Safety Factor
Turbine Blade (material: PC Blend)	Bending from thrust on one blade at 22 m/s*	9.4 N	7.1
Turbine Blade (material: PC Blend)	Centrifugal load at 2740 rpm	8.4 MPa	7.5
Foundation	Tipping from thrust on rotor at 22 m/s**	28.2 N	1.0
Yaw housing set screws	Moment on rotor from thrust force	2.8 N·m	5.0
Pitching linear actuator [14]	Back drive thrust force on linear actuator**	28.2 N	1.6
Brake mount	Von-Mises stress from max rotor torque (Figure 15)	2.7 MPa	23.4
Braking linear actuator [14]	Braking force for maximum rotor torque***	8.73 N	1.37
Shaft bearings	Radial rotor imbalance loads****	10.1 N	247

* The thrust on one blade is approximated as one-third of the maximum theoretical thrust on the rotor, which is 28.19N.

** The theoretical thrust force at 22 m/s was calculated for the operating state, which would be a worst case scenario if the dual pitch and brake mechanisms failed; blades will be feathered and mechanical brake will be engaged past 14 m/s in competition. Thus, these safety factors are conservative.
Thrust at 22 m/s was calculated using the following equation:

$$T = \tfrac{1}{2}\rho A u^2[4a(1 - a)]$$

where T is the thrust force, ρ is the density of air, A is the frontal area of the rotor, u is the wind speed, and a is the axial induction factor. The axial induction factor was conservatively chosen to be 0.33, which is the theoretical maximum. In reality, this value would be lower, decreasing the thrust on the turbine.

*** Maximum wind speed for safety stop is at 11 m/s. The maximum torque at 11 m/s is 0.155 Nm using power (28.6 W) and angular velocity (185.35 rad/s)
The required force at the point of braking is 8.73 N, using disc radius (0.0039 m) and coefficient of friction (0.455 between carbon fiber and aluminum). The braking linear actuator is capable of a 12 N backdrive force.

**** The rotor imbalance was estimated by simplifying each blade as a point mass centered on the blade's center of mass. The center of mass was evaluated on SolidWorks assuming a uniform density throughout the blade. The forces on the blades are given by the following equations:
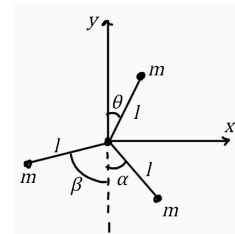
$$R_y = m\omega^2 l(-\sin\theta + \sin\alpha - \sin\beta)$$

$$R_y = 3mg + m\omega^2 l(-\cos\theta + \cos\alpha + \cos\beta)$$

$$R = \sqrt{R_y^2 + R_x^2}$$

where m is the mass of one blade, ω is the rotational speed of the rotor, l is the distance from the rotor center to the blade center of mass, and θ, α, and β are the respective angular positions of each blade.

6.2 Appendix B: Chord/twist optimization and blade geometry from QBlade

	Pos (m)	Chord (m)	Twist	Foil
1	0	0.084	44.7106	FX 63-137 13.7% smoothed
2	0.009	0.0869873	38.935	FX 63-137 13.7% smoothed
3	0.018	0.0872537	33.646	FX 63-137 13.7% smoothed
4	0.027	0.0857682	29.7144	FX 63-137 13.7% smoothed
5	0.036	0.0830114	26.0787	S1221 w/o flap
6	0.045	0.0799989	23.3334	S1221 w/o flap
7	0.054	0.076402	20.7485	S1221 w/o flap
8	0.063	0.0731223	18.7599	S1221 w/o flap
9	0.072	0.0695555	16.8533	S1221 w/o flap
10	0.081	0.0664758	15.361	S1221 w/o flap
11	0.09	0.0632346	13.9073	S1221 w/o flap
12	0.099	0.0604928	12.7527	S1221 w/o flap
13	0.108	0.0576431	11.6126	S1221 w/o flap
14	0.117	0.0552507	10.6957	S1221 w/o flap
15	0.126	0.0527741	9.78001	S1210 12%
16	0.135	0.0506987	9.03587	S1210 12%
17	0.144	0.0485508	8.28563	S1210 12%
18	0.153	0.0467494	7.6705	S1210 12%
19	0.162	0.0448821	7.04529	S1210 12%
20	0.171	0.0440975	6.78705	S1210 12%
21	0.18	0.0433128	6.52881	S1210 12%
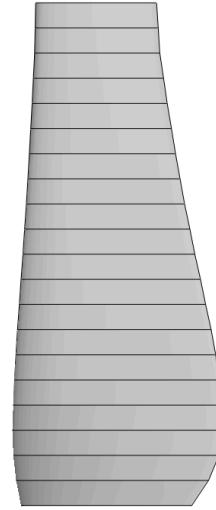
6.3 Appendix C: FEA of revised hub connection geometry of TSR3 blade under centrifugal and bending load at 11m/s
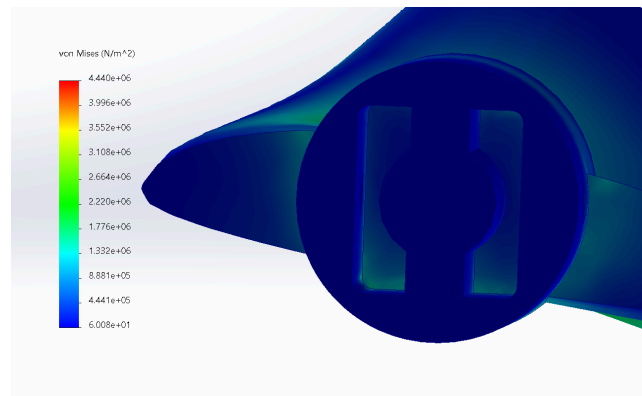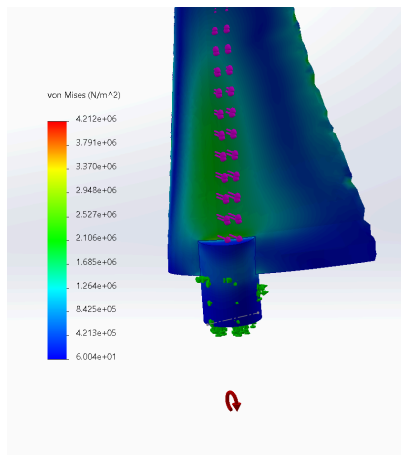
7 References

[1] Low Reynolds Number Airfoil Design Lecture notes. (n.d.).
https://m-selig.ae.illinois.edu/pubs/Selig-2003-VKI-LRN-Airfoil-Design-Lecture-Series.pdf

[2] *Adding winglets on wind turbine blades: Worth the cost?*. Weather Guard Lightning Tech. (2020, October 25). https://weatherguardwind.com/winglets-on-wind-turbine-blades/

[3] Zhao, Z., Jiang, R., Feng, J., Liu, H., Wang, T., Shen, W., Chen, M., Wang, D., & Liu, Y. (2022). Researches on vortex generators applied to wind turbines: A Review. *Ocean Engineering*, *253*, 111266. https://doi.org/10.1016/j.oceaneng.2022.111266

[4] Banggood.com. (n.d.). *JCZK 300C RC helicopter parts main rotor head set*. www.banggood.com. Retrieved April 13, 2023, from
https://usa.banggood.com/JCZK-300C-RC-Helicopter-Parts-Main-Rotor-Head-Set-p-1653921.html?cur_warehouse=CN&fbclid=IwAR0c-LsysOS_x2IZTsrhklhwDU_dwgOQlpMWU4o6zWOufEcoqYrnbVTMS4A

[7] *BL23E48-02.* Lin Engineering. (2022). Retrieved December 8, 2022, from
https://www.linengineering.com/products/brushless-motors/standard-bldc-motors/bl23-series/bl23e48-02/BL23E48-02

[9] DFA90L048017-A (2024). Nanotec. Retrieved April 18, 2023, from DFA90L048017-A - Brushless DC flat motor | Nanotec

[10] Evans, P. (2019, May 30). *Three phase voltage + calculations*.The engineering mindset. Retrieved May 4, 2023, from https://theengineeringmindset.com/three-phase-voltage-calculations/

[11] Keith, J. (2023, January 31). *Capacitor input filter: Formula & calculation: ElectroSchematics*. ElectroSchematics.com. Retrieved May 4, 2023, from
https://www.electroschematics.com/capacitor-input-filter-calculation/

[12] Coduto, D. P., Kitch, W. A., & Yeung, M.-chu R. (2016). *Foundation design: Principles and practices* (3rd ed.). Pearson.

[13] Brower, B. (2010) *Development of Eastern Regional Wind Resource and Wind Plant Output Datasets*. NREL. https://www.nrel.gov/docs/fy10osti/46764.pdf

[14] Actuonix L12 Datasheet F. (2019) Actuonix Motion Devices Inc. Retrieved May 4, 2023, from https://www.actuonix.com/assets/images/datasheets/ActuonixL12Datasheet.pdf